Progress In Electromagnetics Research B, Vol. 76, 87–96, 2017

Advanced Multi-Pass InSAR Imaging for Surface Deformation Studies

Sui Ping Lee*, Yee Kit Chan, and Tien Sze Lim

Abstract—This paper describes a multi-pass InSAR imaging approach for surface deformation studies. Such a technique extends concept of SAR tomography (TomoSAR) based on multi-pass InSAR data, in order to produce deformation map in elevation domain and velocity domain, respectively. Compared to conventional InSAR method, multi-pass InSAR imaging technique acquires multi-baseline information and allows reconstruction of multiple scattering sources in Tomo-Doppler plane (Elevation-Velocity plane). This technique offers a solution to layover issue over conventional InSAR method, but it suffers from double-scattering problem. This paper simulates a phenomenon where double-scattering impairs the imaging process and an improved solution method to separate single and double scatters from inferring pixels. In real circumstance, there are still other interferometric issues such as phase ambiguities of noise and phase discontinuity. Thus, a phase-unwrapping method associated with an improved ordered-statistical filter is included for interferometry processing. An experiment based on real SAR data is set up to demonstrate this technique.

1. INTRODUCTION

Interferometry synthetic aperture radar (InSAR) is a renowned topography measurement technique which employs pairs of SAR images and extracts spatial height information over large scale of illuminated area. Today, almost all portions of earth surface have been modelled into the digital elevation map (DEM) based on InSAR technique via shuttle radar topography mission (SRTM) [1, 2]. Measurement of surface deformation can be done by repeating multiple passes of InSAR imaging process on the same target area. Thus, surface deformation can be detected by comparing these InSAR images with time separation that enables extraction of surface deformation over time, such an approach also known as differential-interferometry synthetic aperture radar (D-InSAR). D-InSAR approach has been widely implemented for deformation mapping. Its applications include and not limited to land use assessment, landslide zone mapping, volcano area monitoring, and ice glacier research [3, 4]. Aforementioned InSAR imaging approaches employ the dominant scattering mechanism by assuming the presence of single scatter on each sample point. However, this assumption could not be hold on the layover area with high density of scatterer such as sharp or vertical terrain slopes and complex building structures, which leads to estimation error. According to the literature [5, 6], such InSAR errors (or referred as InSAR noise) could be significantly improved, if the InSAR height estimation is performed by using multiple baseline information generated from multiple passes of SAR observations. Subsequently, SAR tomography (TomoSAR) [7] emerged as an evolvement technique of InSAR on layover issues migration over recent decade. TomoSAR is able to reconstruct backscattering distribution along elevation profile (slant height) based on multiple passes of InSAR images. Meanwhile, tomographic imaging approach suffers from the issue of multiple scatterers, which might requires research effort for its solutions [8]. In recent years,

Received 20 February 2017, Accepted 5 June 2017, Scheduled 20 June 2017
* Corresponding author: Sui Ping Lee (lee.sui.ping.zte@gmail.com).
The authors are with the Faculty of Engineering and Technology, Multimedia University, Jalan Ayer Keroh Lama, Melaka 75450, Malaysia.

these processing approaches have evolved to more advanced InSAR techniques [9–13]. In this paper, an advanced multiple-passes InSAR imaging approach is proposed for further extended TOMOSAR concept in time domain and not only generates elevation outcome but also extracts velocity information based on multiple passes of InSAR measurement (with multiple spatial and temporal baseline).

It is noted that double-bound scattering problem is unsolvable in TomoSAR [14, 15]. Also, phase ambiguity problem has long been considered as one of the most critical issues in InSAR field [2]. In order to extract more accurate deformation information, advanced multi-pass InSAR imaging techniques attempt to tackle both of aforementioned issues. This paper simulates double-scattering condition and demonstrates possibility to solve double-scattering problem by a simulation model. For real practices, Delaunay Triangular method is applied to data pairing of more than two acquisitions. After pairing, we suggest to include the InSAR model associated with improved order-statistical filter to overcome the phase ambiguity problem due to interferometry processing [14]. After interferometry processing, stack of unwrapped phase images would be rewriten into vector matrix form as collection of received signal. In order to detect multiple scatterers, beam forming estimation is applied by using an inversion matrix. A calibration method based on threshold is employed to adjust deformation images. The final outcome of relevant approach would be an elevation mapping of deformation and a velocity mapping of deformation.

This paper demonstrates the conceptual models and application of an advanced multi-pass InSAR imaging for surface deformation studies. Section 2 describes the imaging process and relevant imaging problem. Section 3 suggests a scheme for actual implementation on real data. Its implementation steps are described. Simulation outcomes of double-scattering and its solution are presented in Section 4. The experimental results based on real data are also discussed in this section. Section 5 concludes the paper.

2. ADVANCED MULTI-PASS INSAR IMAGING AND ITS PROBLEM STATEMENTS

This section describes extension concept of tomography imaging into aforementioned advanced multipass InSAR imaging based on InSAR data analysis. Consider that there is N acquisition of SAR image ($n = N-1$). Thus, t_n indicates time span between two acquisitions (also known as temporal baseline), and b_n refers to the distance of spatial baseline between two acquisitions. Equation (1) shows the signal model of TOMOSAR modelled as superposition of multiple backscatters' sources.

$$S_n = \int_{l_i}^{l_{k-1}} \gamma(l) \exp\left(-j2\pi\xi_n l\right) \, \mathrm{d}l \tag{1}$$

S_n refers to received signal, and γ indicates backscattering coefficient. The slant height or elevation is indicated by l. r denotes target distance from reference track, and λ is wavelength. Spatial frequency can be computed as $\xi_n = \frac{2b_n}{r\lambda}$. Eq. (1) is the Fourier transform of $\gamma(l)$ at ξ_n frequency. It is noted that irregular sample is the main problem of elevation imaging. Equation (2) describes a linear problem after discretization [17].

$$\mathbf{S} = \mathbf{A}\bar{\gamma} \tag{2}$$

By rewriting the relevant variables and parameters after discretization in matrix form: collection of received signal is the vector represented by $\mathbf{S} = [S_0, \ldots, S_{N-1}]^T$, and measured complex data are now indicated by $\bar{\gamma} = [\gamma(l_0), \ldots, \gamma(l_{N-1})]^T$. Elevation is in elevation bin form as l_i where $i = 0, \ldots, k-1$. $\mathbf{A}$ is an $N \times k$ steering vector, $\mathbf{A} = [a(l_0), \ldots, a(l_{k-1})]$ where $a(l_p) = \exp(j2\pi\bar{\varepsilon}l_p)$ and $\bar{\varepsilon} = [\xi_0, \ldots, \xi_{N-1}]^T$.

In order to extract the deformation map, the advanced multipass InSAR technique extends Equation (1) to Equation (3) where deformation term of $d(l, tn)$ is extracted.

$$S_n = \int_{l_i}^{l_{k-1}} \gamma(l) \exp\left(-j2\pi\xi_n l\right) \exp\left(-j\frac{4\pi}{\lambda} d(l, t_n)\right) \mathrm{d}l \tag{3}$$

By further extending $\exp(-j\frac{4\pi}{\lambda}d(l, t_n))$ in Fourier harmonics as Equation (4) with velocity frequency of $\eta_n = \frac{2t_n}{\lambda}$,

$$\exp\left(-j\frac{4\pi}{\lambda} d(l, t_n)\right) = \int_{l_i}^{l_{k-1}} \int_{v_i}^{v_{k-1}} X(l, v) \exp(-j2\pi\eta_n v) dl \; dv \tag{4}$$

Consider that $\gamma(l)X(l,v)$ is substituted into $\gamma(l)$. Thus, received signal of the advanced multipass InSAR imaging approach is modelled as Equation (5)

$$S_n = \int_{l_i}^{l_{k-1}} \int_{v_i}^{v_{k-1}} \gamma(l,v) \exp\left(-j2\pi\left(\xi_n l + \eta_n v\right)\right) dl dv \tag{5}$$

Similar to tomography model, scatterer detection becomes a problem where irregular samples infer on sample pixels. It is necessary to perform two-dimensional Fourier-Inversion to reconstruct backscattering distribution in elevation-velocity plane. Discretization leads to the same linear problem as Equation (2), but its steering model [17] is described as Equation (6) where $\bar{\eta} = [\eta_0, \ldots, \eta_{N-1}]^T$.

$$\mathbf{a}(l_p, v_q) = \exp\left(j2\pi\left(\bar{\xi} l_p + \bar{\eta} v_q\right)\right) \tag{6}$$

In real condition, received signal is always inferred by more scatterers that target detection could be done by analyses on the peaks of backscattering distribution in E-V plane (l, v). Deformation signal is constituted by linear deformation and nonlinear deformation d_{UL} [17].

$$d(l, t_n) = v t_n + d_{\mathrm{UL}}(l, t_n) \tag{7}$$

The estimation error of relevant deformation is considered as e_d. In this scenario, the total estimation error, e_{total}, covers the phase estimation error during InSAR processing, e_{InSAR}. This can be expressed as Equation (8).

$$e_{\mathrm{total}} = e_{\mathrm{d}} + e_{\mathrm{InSAR}} \tag{8}$$

3. EXPERIMENTAL SET UP AND ITS IMPLEMENTATION STEPS

Figure 1 shows the proposed implementation scheme for real data experiment for the multipass InSAR imaging approach with N acquisitions of SAR images. The following paragraph presents the implementation steps of relevant approach. Each acquisition is referred to a single SAR image acquired on certain times pan or path track.

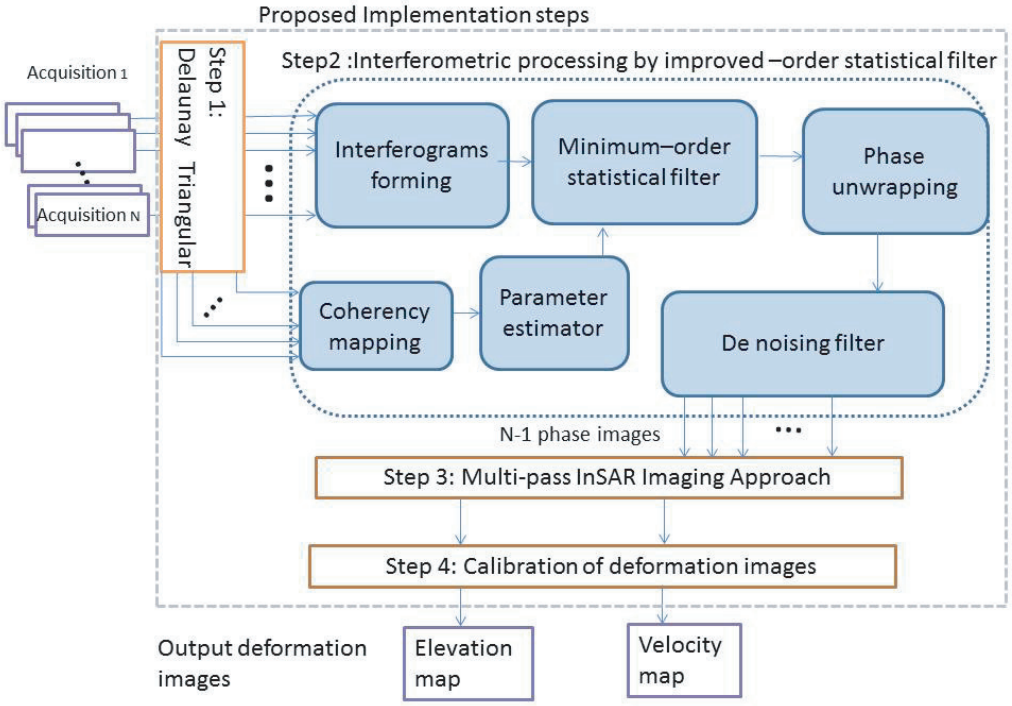

Figure 1. Implementation scheme of advanced multi-pass InSAR imaging.

Step 1: SAR images pairing by Delaunay Triangular method [18]. During interferometry processing, formation of each interferogram requires a pair of SAR images. It is noted that the possible matching combinations are more than $N-1$ though only $N-1$ matched pairs are required in the next step. Thus, pairing process is optimized by referring to a triangular network structure that computes temporal baseline and spatial baseline. The computation outcome distributed in temporal-spatial diagram is shown as Figure 2 where the pairings are selected by referring to the triangular vector among red nodes (red node indicates each acquisition).

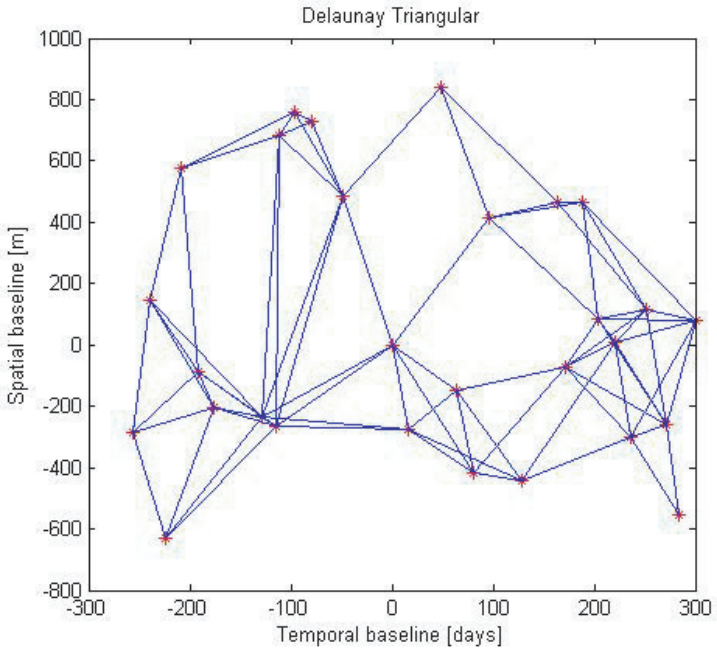

Figure 2. Network structure plotted by Delaunay Triangular.

Step 2: Interferometry processing by improved-order statistical filter. During each pass of operation, decorrelation phenomena due to nonlinear deformation and atmosphere noise create phase ambiguity issue for interferometry processing. However, such a multipass InSAR imaging approach could only be possible with the condition that data stacks are well-compensated. Thus, this step incorporates a phase-unwrapping method associated with an improved order-statistical filter (which is newly developed by [16]) to overcome aforementioned issue. The relevant working mechanisms are as follow. After the pairing of SAR images from Step 1, each interferogram, Φ, is formed by extraction of phase value difference between relevant matched SAR images x_i and x_j.

$$\Phi = \arg(\mathbf{x_i x_j}^*) \tag{9}$$

$()^*$ indicates conjugate value, and arg() refers to arc tangent angle value. Such an interferogram is then filtered by minimum order statistical filter which varies its filtering rate based on the coherency weight, w_c. The coherency weights are determined by the correlation level between x_i and x_j.

$$w_c = \left(\frac{\mid \mathbf{x_i x_j}* \mid}{\parallel \mathbf{x_i} \parallel \parallel \mathbf{x_j} \parallel} \right) \in [0, 1] \tag{10}$$

The larger local window size (3×3) is applied to low coherency area while smaller local window size (1×1) is applied to high coherency area. The pixel value with correlation level less than 0.3 is considered total corrupted since it could not provide useful information [19]. Equation (11) shows an improved-order statistical filter that preserves useful information and restores corrupted pixel (with correlation level lower than 0.3). The minimum order statistical filter [21] sorts pixel values (phase difference) within

its local window and apply restoration based on the minimum value. The local window is denoted by $window_{\Phi}$.

$$f(x,y) = \min_{(x,y)\in window_{\Phi}} \{\Phi(x,y)\}\ ,\ \text{given that, } window_{\Phi} = \begin{cases} \{\Phi(x,y)\} & \text{for} \quad w_c \geqslant 0.3 \\ \left\{ \begin{array}{r} \Phi(x,y), \\ \Phi(x-1,y-1), \\ \Phi(x-1,y), \\ \Phi(x-1,y+1), \\ \Phi(x,y-1), \\ \Phi(x,y+1), \\ \Phi(x+1,y-1), \\ \Phi(x+1,y), \\ \Phi(x+1,y+1) \end{array} \right\} & \text{for} \quad w_c < 0.3 \end{cases} \tag{11}$$

Then, 2D Itoh-based phase unwrapping [20] is implemented into filtered outcome of the minimum ordered-statistical filter for absolute phase estimation. $\hat{\Phi}$ refers to estimated phase value. k_{column} and k_{row} refer to the jump cycle counts adjusted due to adjacent pixel difference in horizontal term and vertical term [19].

$$\hat{\Phi}(x,y) = \Phi(x,y) + 2\pi \left(\sum k_{column}(x,y) + \sum k_{row}(x,y) \right) \tag{12}$$

A first-order neighbour averaging filter (with 3×3 window) is employed for noise suppression purpose. This step repeats $N-1$ times for the interferogram stack and generates $N-1$ outcomes of unwrapped phase image (stack of output images, S). This step has generated stack of enhanced deformation information directly related to spatial difference and mean velocity estimation.

Step 3: Deformation mapping by multi-pass imaging approach. Section 2 describes the imaging process of discretization as Equation (2). To overcome the linear problem after discretization, beam forming can be done by back-projection in Equation (2). The estimation of scattering count $\hat{\gamma}$ is modelled as Equation (13) where $()^H$ refers to Hermitian.

$$\hat{\gamma} = \mathbf{A}^H \mathbf{S} \tag{13}$$

Since the estimation model of backscatters is considered as a function responding to elevation and velocity [21], maximum value of estimated scatterer becomes the main reference to generate the elevation map, l, and velocity map, v. Such a process can be modelled into a normalized correlation term as Equation (14).

$$C = \max_{l,v} \left(\frac{\mid \mathbf{a}^H \mathbf{S} \mid}{\parallel \mathbf{a}^H \parallel \parallel \mathbf{S} \parallel} \right) \in [0,1] \tag{14}$$

Step 4: Calibration of deformation map. By referring to the correlation term of Equation (14), two deformation images which cover an elevation map and a velocity map can be extracted as follows.

$$(\hat{l}, \hat{v}) = \arg \left[\max_{l,v} \left(\frac{\mid \mathbf{a}^H \mathbf{S} \mid}{\parallel \mathbf{a}^H \parallel \parallel \mathbf{S} \parallel} \right) \right] \tag{15}$$

These images may still contain noise on the low coherency area, i.e., the place with high density scatterers such as vegetation and road with moving vehicles. In order to establish ready-to-use outcomes for surface deformation studies, the noisy and less accurate part should be removed. Such calibration can be easily done by setting up a threshold filter to filter out unwanted information based on its coherency level.

$$C \gtrless \text{Threshold} \in [0,1] \tag{16}$$

The relevant threshold is set by referring to desired value of false alarm probability, PFA under following hypotheses test.

$$\begin{aligned} H_0 &: S = w \\ H_1 &: S = \gamma_1(l) a(l_1, v_1) + \gamma_2(l) a(l_2, v_2) + w \end{aligned} \tag{17}$$

The initial hypothesis H_0 refers to the circumstance of only background noise (without presence of any scatterer) where w indicates $N \times k$ disturbance samples modelled as zero mean complex circular Gaussian as stated in [22]. The alternative hypothesis test H_1 shows the presence of double scatterers with noise. In order to detect the targets without background noise, H_0 is tested against the alternative, $\bar{H_0}$. P_{FA} is defined as below.

$$P_{FA} = P\left(\bar{H_0} \mid H_0\right) = P\left(C \geqslant \text{Threshold} \mid H_0\right) \tag{18}$$

It is noted that the false alarm probabilities can be very different and varying on different data sets. Thus, the threshold can also be empirically set for many cases of real data experiment.

The working principal of double scatterers detection approach is described as above where an inversion matrix (Equation (13)) is applied to reconstruct target scatterers. If above working steps are implemented without the choice of inversion matrix (by skipping Equation (13)), the correlation term will be compared to a threshold that identifies single scatterer. Such procedures form a technique similar to standard permanent scatterer identification (PSI), but it is framed in advanced multi-pass imaging approach [23].

4. RESULTS AND ANALYSES

4.1. Simulation Results

This section presents the simulation result in noise free condition. Figure 3 shows a simulation model of beam forming process where back scatterer is reconstructed to a function of elevation and velocity. Figure 4 shows simulation results of double-scattering mechanism of two different height targets. Target scatters could be well-estimated and separated from double-scatter mechanism in the first simulation scene of Figure 4. The second simulation scene of Figure 4 shows an estimation error case of double-scattering. This is because the target heights between two these scatters is too close to be over the limit of baseline resolution. Thus, this is the constraint of the current solution model.

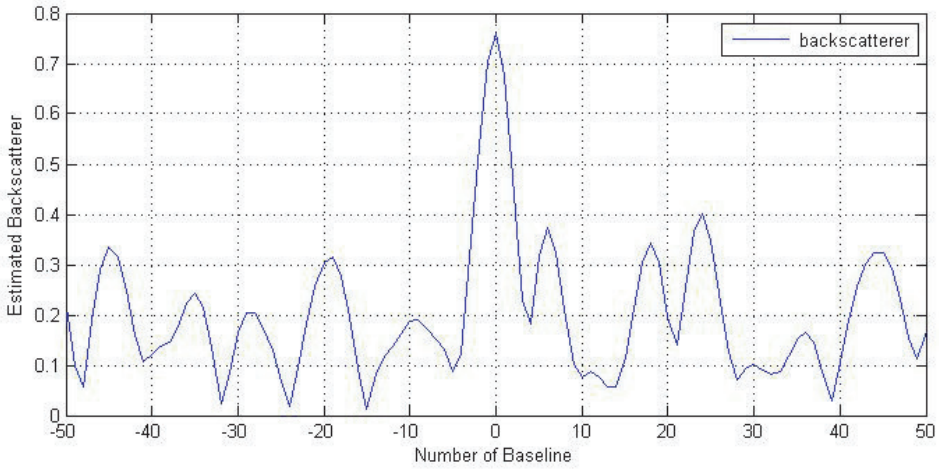

Figure 3. Simulation of beam forming.

4.2. Experimental Results Based on Real Data

The experimental results based on real SAR data are shown in this section. The input data are constituted of 29 acquisitions of SAR observations on the same target area. The master image of the SAR acquisition is shown in Figure 5, which is the street view from satellite radar on Rome, Italy. Both Figure 6 and Figure 9 show coherency mapping of input data stacks on step 3 (based on single-scatterer and double-scatterer detections, respectively). Figure 7 and Figure 8 display deformation map (in term of elevation and velocity) via single-scatterer detection. The advanced multi-pass InSAR

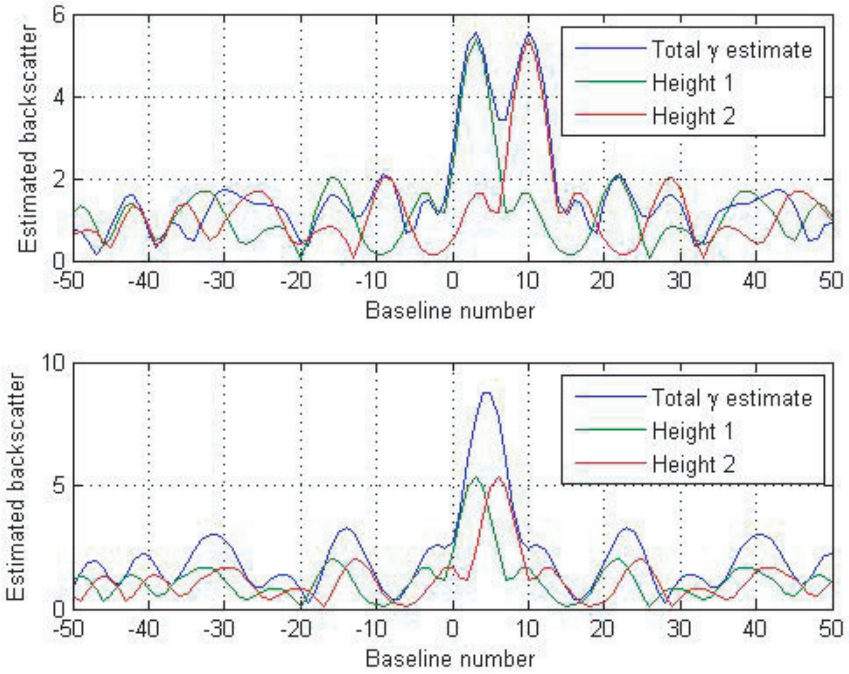

Figure 4. Solution model for double-scattering and its constraint.

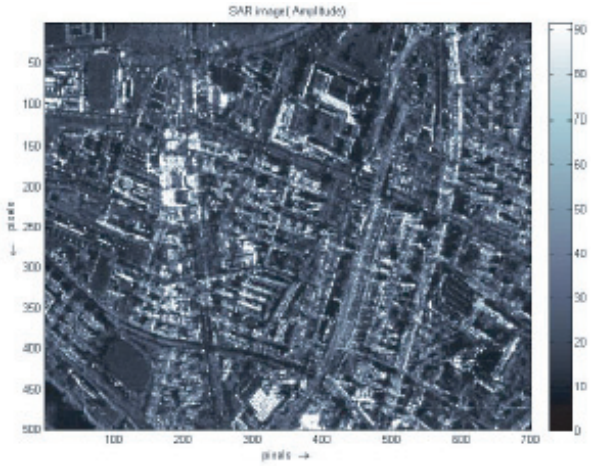

Figure 5. Real data image of SAR observation on target area.

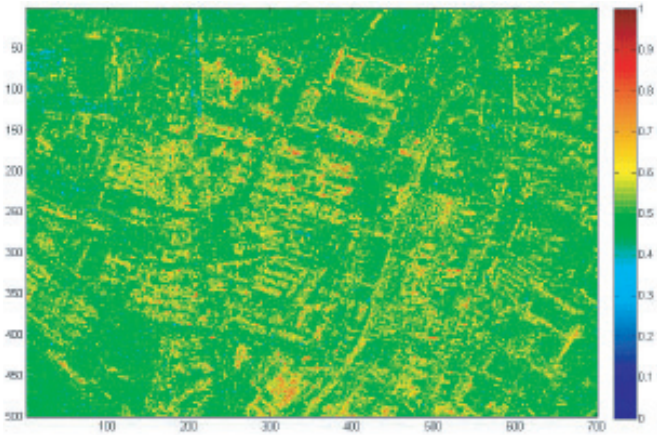

Figure 6. Correlation mapping based on single scatterer detection.

imaging techniques refer to an image extraction approach based on double-scatterer detection, and its outcomes of deformation map are displayed in elevation term (Figure 10) and velocity term (Figure 11) as well.

From the amplitude image (Figure 5) and coherence image (Figure 6), we can observe that stationary building area and concrete infrastructure show high correlation index above 0.6 while the roads' busy traffic shows low correlation index. In this experiment, we focus on observing the hard construction buildings. Thus, busy walking streets paths and roads with traffic will be considered as background noise. 0.6 is considered as the threshold value for false alarm probability. As a result, we can notice that all of the road area with moving traffic is totally filtered away during calibration step.

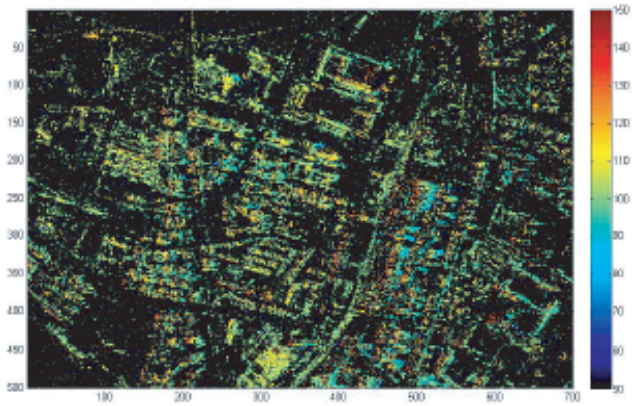

Figure 7. Deformation map in elevation based on single scatterer detection.

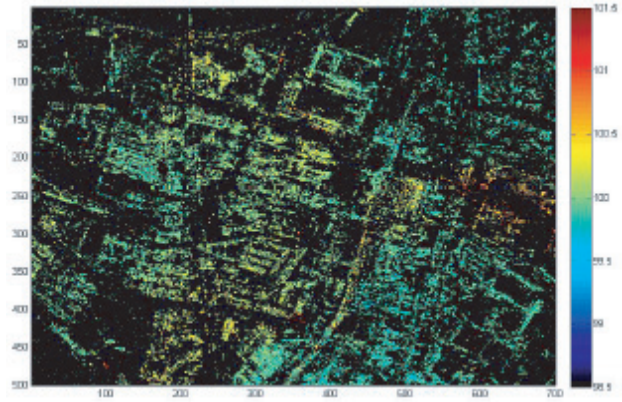

Figure 8. Deformation map in velocity based on single scatterer detection.

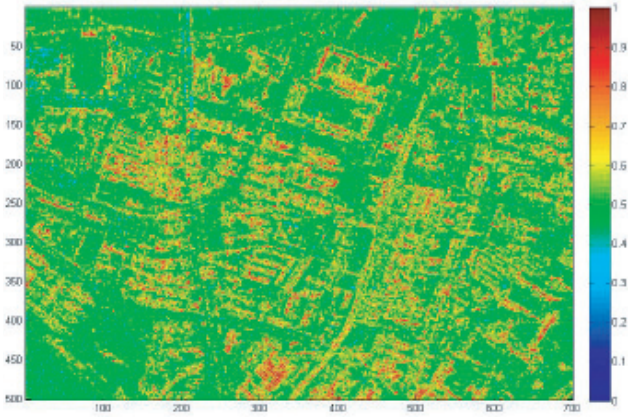

Figure 9. Correlation mapping based on double scatterers detection..

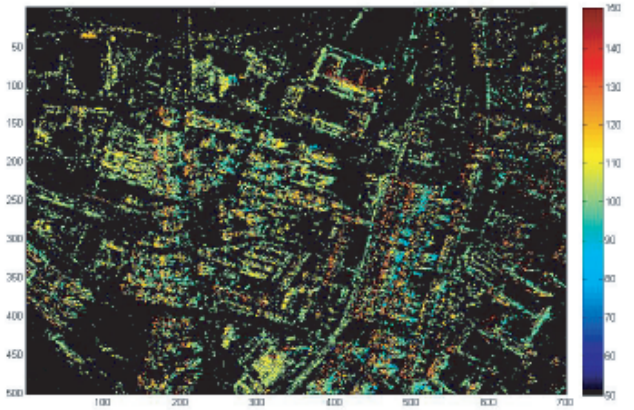

Figure 10. Deformation in elevation based on double scatterers detection.

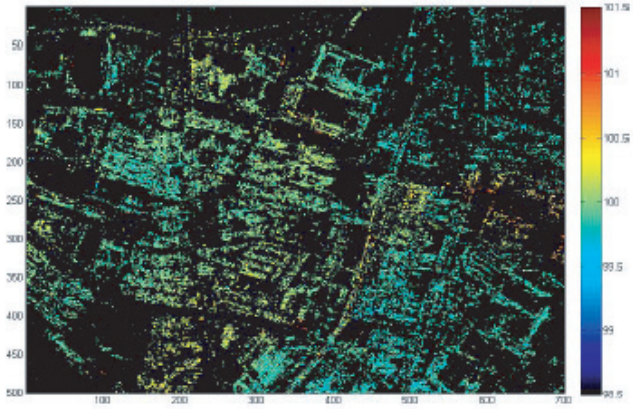

Figure 11. Deformation in velocity based on double scatterers detection.

Based on the processing outcomes, correlation map of double-scatterer detection (Figure 9) shows higher correlation level than correlation map of single-scatterer detection (Figure 6). From Figure 7 and Figure 8, we can still observe that the noise whereby the noise level is high on low coherency area (the

darker part of coherency map of Figure 6). Compared with Figure 10 and Figure 11 (double-scatterer detection), the quality of single-scatterer detected deformation images seems degraded. Overall, the images generated by double-scatterer detection increase sensitivity level of similarity index and yield outcome images with better accuracy.

In these deformation images, red colour part indicates the area with higher deformation rate while deep blue indicates slow or stationary deformation. From the elevation map, we discover that the red colour areas are mostly formed by the place with vegetation. Since the vegetation areas contribute to high volume of scatters, the portion of red colour indicates inferring source (instead of fast surface deformation). Figure 11 of velocity map presents the velocity information of surface deformation on buildings. Apparently, such an imaging technique works better on stationary buildings and concrete infrastructure.

5. CONCLUSION

The modelling process of advanced multi pass InSAR is described in this paper. The issues of double scatterings are investigated, and a solution method is simulated. A scheme is proposed when the implementation steps are described. The real data experiment based on double scatterers detection is demonstrated for deformation mapping. Compared to single-scatterer detection, advanced multi-pass approach can provide InSAR outcome images with better accuracy. Such techniques are also appropriate for being applied to buildings or bridge monitoring.

ACKNOWLEDGMENT

The authors would like to thank the reviewers for valuable comments and express the gratitude to Diego Reale and Gianfranco Fornaro for providing real satellite data training through International Summer School on Radar/SAR 2016, organised by Fraunhofer Institute.

REFERENCES

1. Massonnnet, D. and K. L. Feigl, "Radar interferometry and its application to changes in earth surface," *Rev. Geophsys.*, Vol. 36, No. 4, 441–500, Nov. 1998.
2. Roland, B., P. A. Rosen, and E. J. Fielding, "Synthetic aperture radar interferometry to measure Earth's surface topography and its deformation," *Annu. Rev. Earth Planet. Sci.*, Vol. 28, 169–209, May 2000.
3. Rosen, P. A., S. Hensley, I. R. Joughin, S. N. Madsen, E. Rodriguez, and R. M. Goldstein, "Synthetic aperture radar interferometry," *Proceeding of IEEE*, Vol. 88, No. 3, Mar. 2000.
4. Tough, R. J. A., "Interferometric detection of sea surface features," *Signals and Radar Establishment*, memorandum 4446, UK, 1991.
5. Wu, B. I., M. C. Yeuing, Y. Hara, and J. A. Kong, "Insar heigh inversion by using 3-D phase projection with multiple baselines," *Progress In Electromagnetics Reseach*, Vol. 91, 173–193, 2009.
6. Ren, X. Z., L. H. Qiao, and Y. Qin, "A three-dimensional imaging algorithm for tomography SAR based on improved interpolated array transform1," *Progress In Electromagnetics Research*, Vol. 120, 181–193, 2011.
7. Gini, F., F. Lombardini, and M. Montanari, "Layover solution in multibaseline SAR interferometry," *IEEE Trans. Aerosp. Electron. Syst.*, Vol. 38, No. 4, 1344–1356, Oct. 2002.
8. Zhang, W., "Two-dimensional microwave tomographic algorithm for radar imaging through multilayered media," *Progress In Electromagnetics Research*, Vol. 144, 261–270, 2014.
9. Lombardini, F., "Differential tomography: A new framework for SAR interferometry," *IEEE Trans. Geosci. Remote Sens.*, Vol. 43, No. 1, 37–44, Jan. 2005.
10. Reale, D., G. Fornaro, A. Pauciullo, X. Zhu, and R. Bamler, "Tomographic imaging and monitoring of buildings with very high resolution SAR data," *IEEE Geosci. Remote Sens. Lett.*, Vol. 8, No. 4, 661–665, Jul. 2011.

11. Reale, D., D. O. Nitti, D. Peduto, R. Nutricato, F. Bovenga, and G. Fornaro, "Postseismic deformation monitoring with the COSMO/SKYMED constellation," *IEEE Geosci. Remote Sens. Lett.*, Vol. 8, No. 4, 696–700, Jul. 2011.
12. Fornaro, G., A. Pauciullo, and F. Serafino, "Deformation monitoring over large areas with multipass differential SAR interferometry: A new approach based on the use of spatial differences," *International Journal of Remote Sensing*, Vol. 30, No. 6, 1455–1478, Apr. 2009.
13. Berardino, P., G. Fornaro, R. Lanari, and E. Sansosti, "A new algorithm for surface deformation monitoring based on small baseline differential SAR interferograms," *IEEE Trans. Geosci. Remote Sens.*, Vol. 40, No. 11, 2375–2383, Nov. 2002.
14. Fornaro, G., D. Reale, and F. Serafino, "Four-dimensional SAR imaging for height estimation and monitoring of single and double scatterers," *IEEE Trans. Geosci. Remote Sens.*, Vol. 47, No. 1, 224–237, Jan. 2009.
15. Solimene, R., A. Brancaccio, R. Di Napoli, and R. Pierri, "3D sliced tomographic inverse scattering experimental results," *Progress In Electromagnetics Research*, Vol. 105, 1–13, 2010.
16. Lee, S. P., Y. K. Chan, T. S. Lim, and V. C. Koo, "An InSAR phase estimation method for surface derformation studies," *International Conference on Space, Aeronautical and Navigational Electronics 2016, IEICE Tech. Rep.*, Vol. 116, No. 319, 109–114, SANE2016-73, Nov. 2016.
17. Reale, D., G. Fornaro, and A. Pauciullo, "Extension of 4-D SAR imaging to the monitoring of thermally dilating scatterers," *IEEE Trans. Geosci. Remote Sens.*, Vol. 51, No. 12, Dec. 2013.
18. Mora, O., J. J. Mallorqui, and A. Broquetas, "Linear and nonlinear terrain deformation maps from a reduced set of interferometric SAR images," *IEEE Trans. Geosci. Remote Sens.*, Vol. 41, No. 10, 2243, 2253, 2003.
19. Wei, M. and T. Sandwell, "Decorrelation of L-band and C-band interferometry over vegetated areas in california," *IEEE Trans. Geosci. Remote Sens.*, Vol. 48, No. 7, 2942–2952, 2010.
20. Ghighlia, D. C. and M. D. Pritt, *Two-Dimensional Phase Unwrapping: Theory,Algorithms, and Software*, 1st Edition, Wiley-Interscience, New York, 1998.
21. Stella, A. and B. Trivedi, "Implementation of order statistic filters on digital image: A comparative study," *International Journal of Modern Engineering Research*, Vol. 2, No. 5, 3143–3145, 2012.
22. De Maio, A., G. Fornaro, and A. Pauciullo, "Detection of single scatterers in multidimensional SAR imaging," *IEEE Trans. Geosci. Remote Sens.*, Vol. 47, No. 7, 2284–2297, Jul. 2009.
23. De Maio, A., G. Fornaro, A. Pauciullo, and D. Reale, "Detection of double scatterers in SAR tomography," *IEEE International Geoscience and Remote Sensing Symposium, IGARSS 2009*, Vol. 3, III-172, IEEE, Jul. 2009.